

RePAST: A ReRAM-based PIM Accelerator for Second-order Training of DNN

Yilong Zhao¹, Li Jiang¹, Mingyu Gao², Naifeng Jing¹, Chengyang Gu¹, Qidong Tang¹,
Fangxin Liu¹, Tao Yang¹, Xiaoyao Liang^{1*}

¹School of Electronic Information and Electrical Engineering, Shanghai Jiaotong University, Shanghai, China

² Institute for Interdisciplinary Information Sciences, Qinghua University, Beijing, China

sjtuzy1@sjtu.edu.cn jiangli@cs.sjtu.edu.cn gaomy@tsinghua.edu.cn

{sjtuj, zeb19980914, tangqidong, liufangxin, yt594584152}@sjtu.edu.cn liang-xy@cs.sjtu.edu.cn

Abstract—The second-order training methods can converge much faster than first-order optimizers in DNN training. This is because the second-order training utilizes the inversion of the second-order information (SOI) matrix to find a more accurate descent direction and step size. However, the huge SOI matrices bring significant computational and memory overheads in the traditional architectures like GPU and CPU. On the other side, the ReRAM-based process-in-memory (PIM) technology is suitable for the second-order training because of the following three reasons: First, PIM’s computation happens in memory, which reduces data movement overheads; Second, ReRAM crossbars can compute SOI’s inversion in $O(1)$ time; Third, if architected properly, ReRAM crossbars can perform matrix inversion and vector-matrix multiplications which are important to the second-order training algorithms.

Nevertheless, current ReRAM-based PIM techniques still face a key challenge for accelerating the second-order training. The existing ReRAM-based matrix inversion circuitry can only support 8-bit accuracy matrix inversion and the computational precision is not sufficient for the second-order training that needs at least 16-bit accurate matrix inversion. In this work, we propose a method to achieve high-precision matrix inversion based on a proven 8-bit matrix inversion (INV) circuitry and vector-matrix multiplication (VMM) circuitry. We design RePAST, a ReRAM-based PIM accelerator architecture for the second-order training. Moreover, we propose a software mapping scheme for RePAST to further optimize the performance by fusing VMM and INV crossbar. Experiment shows that RePAST can achieve an average of $115.8 \times / 11.4 \times$ speedup and $41.9 \times / 12.8 \times$ energy saving compared to a GPU counterpart and PipeLayer on large-scale DNNs.

I. INTRODUCTION

Most prevalent optimizers for neural network training, including Stochastic Gradient Descent (SGD) [38], Adagrad [13] and Adam [23], only use the information of the first-order gradient. However, as the complexity of the neural network model increases, these optimizers take much more time to train the neural network. For example, it takes over 29 hours to train a ResNet-50 on an 8-GPU cluster [17]. To address the problem, second-order training algorithms are proposed to accelerate the training process [24], [31], [36]. These algorithms take advantage of the inverse of the second-order information (SOI) matrix to accelerate the convergence. For the common second-order optimization methods, e.g. Newton method and natural gradient method, their SOI matrices are Hessian Matrix (HM) and Fisher Information Matrix (FIM), respectively. For

small neural networks on small datasets, such as autoencoder on MINST, second-order training can reduce the iteration number by over $100 \times$ [31]. One major challenge of directly performing the two algorithms on large-scale DNNs is that the SOI size increases quadratically as the parameter number increases. For example, a ResNet-50 network has 2.5×10^7 parameters, and the size of its HM will be around 6.3×10^{14} . The large size of SOI brings the following two problems: First, computing with SOI requires a significant amount of data movement. Second, the complexity of matrix inversion on SOI is $O(n^3)$, which causes a prohibitive computational cost. As a result, directly applying the second-order algorithms to DNNs in reality is actually much slower than the first-order algorithms.

Current second-order training algorithms approximate the SOI into several smaller matrices to reduce the overhead brought by SOI. They treat the elements across different layers as 0. K-FAC algorithm uses Kronecker decomposition to decompose the FIM of each layer into two smaller matrices [31]. However, the size of SOI is still large. For example, after this approximation, the size of SOI is still about 1.4×10^8 for ResNet-50. ADAHESSIAN directly approximates the SOI into a diagonal matrix so that we do not need to invert the SOI matrix [51]. However, this results in a large computational error such that little improvement in the convergence rate for the training process is observed. Some algorithms trade off the overhead of SOI and the convergence rate, by approximating the SOI matrix into a block-diagonal matrix [7], [49]. However, limited by the GPU performance, the optimal block size is usually small. For example, the optimal block size of THOR algorithm is only 128 [7]. With smaller block sizes, it takes more epochs to train due to higher approximate errors, causing longer convergence time, offsetting the algorithmic advantage of the second-order training.

ReRAM-based PIM is an emerging technique whose computation happens in the memory and has the inherent ability to accelerate vector-matrix multiplication (VMM) [21]. While each ReRAM cell can only differentiate a limited number of bit levels, which means the ReRAM crossbar itself can only perform low-precision VMM computation, high-precision VMM can be carried out by splitting it into multiple low-precision VMMs with bit-slicing scheme [41]. Based on this,

Song et al. propose Pipelayer, a ReRAM-based architecture to accelerate the first-order training of DNN [44]. The ReRAM crossbar can also accelerate the computation of matrix inversion (INV), such as the design proposed by Sun et al. [47]. The time complexity of their circuit is $O(1)$. But the precision is still limited by the number of bits that the ReRAM cell can support. The authors in [14] propose an analog bit-slicing scheme and increase the precision of INV circuit to 8-bit. They use analog amplifiers and combine the analog signals from bitlines into a more precise analog signal. However, the method can not further improve the precision of the INV circuit because the noise level has surpassed the limit of the precision in the analog signals.

The characteristic of ReRAM-based PIM technology makes it suitable for accelerating the second-order training algorithms. PIM can reduce the data movement of the large SOI and PIM can perform the matrix inversion in $O(1)$ time regardless of the matrix size, reducing the computational overhead of matrix inversion. Also, ReRAM-based crossbars can perform high-precision VMM through the bit-slicing technique. However, the key challenge in designing PIM accelerators for the second-order training algorithms is that the current PIM matrix inversion circuit can only support up to 8-bit precision. This cannot meet the criterion for the second-order training algorithms, most of which require 16-bit precision or higher [7], [15], [31], [49].

In this work, we address this challenge and propose RePAST, a ReRAM-based PIM accelerator for the second-order training. We make the following contributions:

- We propose a novel scheme to implement the high-precision matrix inversion based on multiple low-precision matrix inversion circuit. Leveraging Taylor Expansion, a high-precision matrix inversion can be decomposed into a series of low-precision matrix inversions chained with a VMM operation, both of which can be implemented with ReRAM-based crossbars.
- We propose RePAST, a ReRAM-based accelerator architecture for the second-order training. The RePAST has a series delicate architecture design and mapping strategy to fuse INV and VMM operations smoothly that can support all the typical operations in the second-order training algorithms, including VMM and high-precision INV.
- The mapping strategy can also reduce the overhead of SOI matrix. We find that some patterns in the dataflow graph vary in computation latency or memory footprint if we choose different mapping strategies. For each pattern, we propose a method to select the optimized mapping strategy for different layers.

The remainder of the paper is organized as follows: Section II introduce the background of the second-order training algorithms and ReRAM-based VMM and low-precision INV circuits. In Section III, we introduce a novel method for the high-precision matrix inversion and implement it based on the ReRAM-based VMM and low-precision INV circuits. Section

IV presents the overview and the hardware design of the RePAST architecture. In Section V, the mapping scheme is explained. Section VI presents the evaluation and analysis of RePAST. Section VII discusses other related works. Section VIII concludes the paper.

II. BACKGROUND

A. Second-Order Training

First-order training algorithms only utilize the first-order information to obtain the direction and step for optimization. The rule for parameter update is:

$$\theta = \theta - \eta \cdot \nabla_{\theta} J(\theta) \quad (1)$$

where θ is the parameter of neural network, J is the loss function, and η is the learning rate.

Second-order training methods take advantage of the SOI matrix H to obtain a better descent direction and step. Since the SOI matrix depicts the surrounding landscape, the descent path is closer to the optimal descent path and can avoid getting stuck in the saddle point. As a result, the convergence is faster and the number of iterations and epochs can be reduced. For example, the second-order optimizer proposed in [36] only needs half of the iterations or epochs to train a ResNet-50 compared to the first-order one. The rule of parameter update in the second-order training is:

$$\theta = \theta - \eta \cdot H^{-1} \nabla_{\theta} J(\theta) \quad (2)$$

where H is derived from J , and θ , decided by the definition of SOI. However, this formulation cannot be directly implemented for DNN. This is because the size of SOI scales quadratically with the number of parameters, which results in unacceptably large overheads for both computation and storage. Therefore, most algorithms decouple the full SOI matrix by layers, regarding the second-order gradient between layers as 0. We introduce two popular approaches below:

1) *K-FAC Algorithm*. K-FAC is derived from Natural Gradient method (NG), whose SOI is the Fisher information matrix (FIM) \mathcal{F} [31]. K-FAC decomposes each layer's FIM block into the Kronecker product of two small matrices A and G , which are much smaller than the original FIM. After the approximation and decomposition, the storage of the ResNet-50 SOI becomes 140 million, still large but acceptable for GPU. Moreover, the Kronecker product can be transformed into matrix multiplication. Therefore the parameter update rule becomes:

$$\theta = \theta - \eta \cdot A^{-1} \nabla_{\theta} J(\theta) G^{-1} \quad (3)$$

The matrix A and G are obtained by $A = a \cdot a^T$ and $G = g \cdot g^T$, where a is the input feature map and g is the gradient of the layer. Therefore, the two SOIs can be obtained during the backpropagation efficiently. In the fully connection layer (FC), the input feature map a and gradient g are directly multiplied with themselves when computing A and G . While for convolution layer, a and g are firstly reshaped to $c_{in}k^2 \times hw$ and $c_{out} \times hw$ respectively, and

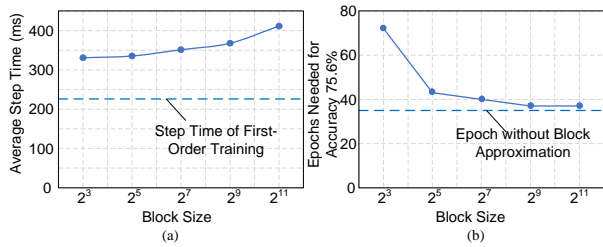


Fig. 1. With different block sizes, (a) the step time of training ResNet-50 on GPU, and (b) the epoch number of training ResNet-50 to 75.6% accuracy. The epoch number of ResNet-50 training without block approximation is 34 [36].

then multiplied with themselves, where c_{in} , c_{out} , k , h and w are input/output channel, kernel size, height and width of the feature map, respectively. Therefore, for convolution layer, $A \in \mathbb{R}^{c_{in}k^2 \times c_{in}k^2}$ and $G \in \mathbb{R}^{c_{out} \times c_{out}}$ [36].

2) *Gauss-Newton Algorithm*. Gauss-Newton method is derived from the Newton method, whose SOI is the Hessian matrix (HM) \mathcal{H} [24], [49]. Each layer’s HM block is approximated by $H \approx \nabla_{\theta} J(\theta) B \nabla_{\theta} J(\theta)^T$, where the matrix B is decided by the loss function. For example, when using cross entropy loss, B becomes the identity matrix.

Diagonal block approximation of SOI matrices. Nevertheless, even with the approximation in both algorithms, the computation of SOI is still a large overhead. Therefore, some works further approximate FIM and HM into block-diagonal matrices [7], [49] or even diagonal matrices [51]. Therefore, the inversion of SOI matrix can be obtained by inverting each blocks, and reduce the computational overhead. Take one convolution layer of ResNet-50’s conv5_x as an example. The layer has 512 output channels, therefore, the matrix G is 512×512 according to [36]. If we approximate G into four 128×128 diagonal blocks, the storage is reduced by $4\times$. Moreover, as the computational complexity of matrix inversion is $O(n^3)$, after approximation, the computing is reduced by $64\times$. Fig. 1(a) plot the step time of ResNet-50 training with different block sizes. Using a smaller block size can reduce the execution time of SOI. However, a small block size also means that more information in SOI has been discarded and the descent direction and step size may not be accurate. This will actually slow down the overall convergence process in training because it requires more training epochs to converge. As Fig. 1(b) shows, the required epoch number of ResNet-50 training increases sharply with a shrinking block size. Therefore, this approximation introduces a trade-off between the convergence rate and block size. In [7], the result shows that a block size of 128 should be suitable for a GPU. However, such a block size may slow down the convergence by 29.4% and diminish the advantage of the second-order training.

B. PIM-Based VMM and Matrix Inversion

Current works show that ReRAM-based crossbars offer great efficiency in computing vector-matrix multiplication (VMM) with PIM technologies [21]. One such ReRAM-based VMM accelerator is illustrated in Fig. 2(a). The matrix element values are programmed (i.e. written) into the crossbar,

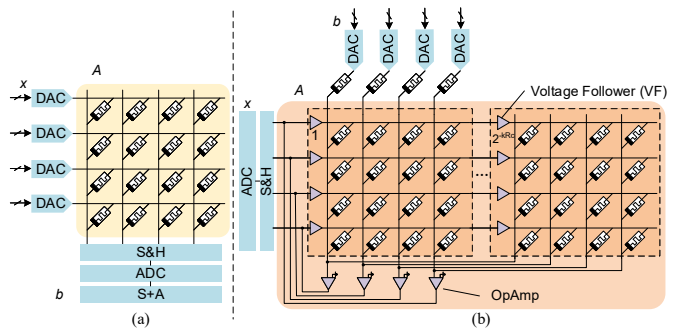


Fig. 2. ReRAM crossbar circuits for accelerating (a) vector-matrix multiplication (VMM) and (b) matrix inversion (INV).

and the input vector is applied to the wordline as voltage levels through DACs. According to the Kirchhoff’s Law, the aggregated currents on the bitlines, after passing through ADCs, become the result of the VMM. DNN inference and training require sufficient precision for VMM operations, e.g., 8-16 bits. However, the state-of-the-art ReRAM cell can only handle 2-6 bits [20]. Therefore, each element of the matrix is split by bits and written to several adjacent cells. Moreover, the DAC’s complexity is exponential to the resolution. To allow for low-bit DACs, each input vector element is also split by bits and applied to a wordline across several cycles. The intermediate results across bitlines and cycles are combined into the final result by shift-and-add operation (S+A). This is the well-known *bit-slicing* scheme to solve the precision problem in VMM [9], [41].

Recent works also use ReRAM crossbars to accelerate matrix inversion (INV) with the help of extra analog components [14], [45], [47]. The circuit is shown in Fig. 2(b). Suppose a matrix A is Q_A -bit quantized, and a ReRAM cell has R_c bits. A is bit-sliced and each slice is programmed to a separate ReRAM crossbar. The i^{th} ReRAM crossbar’s voltage followers’ (VFs’) gain is set to 2^{-iR_c} . A vector $-b$ is applied as voltage levels on the bitline resistances of the crossbar. The currents on the bitlines of the crossbars are aggregated, and are fed back with open-loop operational amplifiers (OpAmps) to the wordlines. According to the virtual short and virtual open characteristic of the OpAmps, the voltages on the wordlines would converge to the values that make both the current and voltage on the bitlines to 0. Then the wordline voltage x , A and the bitline voltage b will satisfy Eqn. 4, effectively achieving a matrix INV in Eqn. 5:

$$x \cdot A = b \quad (4)$$

$$x = A^{-1} \cdot b \quad (5)$$

The convergence time is decided by the dynamic characteristic of the OpAmps. If the OpAmp has a wider bandwidth, the convergence is faster. If we can keep the convergence time within one cycle, the circuit can compute the matrix inversion in $O(1)$ time. For example, the circuit in [14] can converge within 50ns, much shorter than the cycle time for PIM architectures (typically around 100ns [41]).

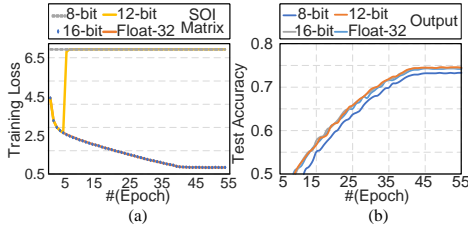


Fig. 3. (a) Loss curve when training ResNet-50 with 8-bit, 12-bit and 32-bit (full-precision) second-order information (SOI) matrices. (b) The test accuracy in ResNet-50 with different quantization levels to the result of matrix inversion, which shows that 16-bit result is sufficient for second-order training.

Although such ReRAM-based INV circuitry has been recently proposed to compute matrix inversion, its precision is still quite limited and cannot meet the requirement of DNN training. Fig. 3(a) depicts the training loss curve when training ResNet-50 [17] with 8-bit, 12-bit, 16-bit and full-precision SOI matrix using the same learning rate. Training with 8-bit and 12-bit SOI matrix results in non-convergence. This is because the SOI matrix’s elements are small values, and quantization errors may lead to large deviations in the matrix inversion results. The requirement of SOI matrix precision is at least 16-bit. This precision exceeds the limit of existing matrix inversion circuitry [14], [45], [47]. Fig. 3(b) depicts the test accuracy with different quantization levels to the result of matrix inversion. A less accurate matrix inversion result also degrades the training effect. At least 16-bit accurate matrix inversion result is required. Meanwhile, the precision of x and b is limited by ADC and DAC resolution, respectively. Although the matrix A is programmed to multiple crossbars, the precision of A can be heavily limited by the noise on the bitlines. For example, [14] only supports a matrix inversion for 8-bit accuracy, with a 6-bit input b and an 8-bit output x , and can only be used as one preconditioner. Note that unlike VMM, the INV circuit does not allow a bit-slicing scheme, because matrix inversion does not have a distributive law.

III. HIGH-PRECISION MATRIX INVERSION

A. The Algorithm for High-Precision Matrix Inversion

Given a matrix A and a vector b , matrix inversion aims to solve $x = A^{-1} \cdot b$. We denote the numbers of bits for the three quantized values as Q_A , Q_b , and Q_x , respectively. Second-order training usually requires high-precision quantizations, e.g., $Q_A = 16$, $Q_b = 16$, and $Q_x = 16$. The resolution of DAC, ADC, and the number of bits a ReRAM cell can support is denoted as R_{DAC} , R_{ADC} and R_c . We connect n crossbars together by VFs as [14] does as shown in Fig. 2(b). Hence, the k crossbars can work together for INV of a $(k \cdot R_c)$ -bit matrix A . However, due to the noise impact in analog circuits, constructing a 16-bit matrix A is not realistic. Moreover, the resolutions of DAC and ADC still limit the precision of x and b . To address these issues, we propose a novel scheme for the INV circuit in this subsection. The scheme can be divided into 3 steps, for b , x , and A , respectively:

1) *Bit-slicing scheme for input b* . For vector b , we can slice it into $N_b = \lceil Q_b / R_{DAC} \rceil$ slices, with each slice having R_{DAC}

bits. Thus, $b = \sum_{i=0}^{N_b-1} b_i \cdot 2^{i \cdot R_{DAC}}$, where b_i is the i^{th} slice of b . We have:

$$x = A^{-1} \cdot b = \sum_{i=0}^{N_b-1} (A^{-1} \cdot b_i) \cdot 2^{i \cdot R_{DAC}} \quad (6)$$

Therefore, we can first calculate the matrix inversion on each slice of b and then “shift-and-add” (S+A) the partial results to obtain the final result.

2) *Bit-slicing scheme for output x* . For the output vector x , the analog signals converged on the bitlines actually contain the complete information. But due to ADCs’ limited resolution, only the first R_{ADC} bits can be quantized to digital values. Therefore, we repeat the following steps iteratively until all the bits are quantized by the ADCs. In the j^{th} iteration, one vector b_j is applied to DAC and the result is quantized by the ADCs as x_j . We will then compute $b_{j+1} = (b_j - A \cdot x_j) \cdot 2^{R_{ADC}}$. After that, we repeat the loop, applying b_{j+1} to DAC to obtain the next R_{ADC} bits of x . After $\lceil Q_x / R_{ADC} \rceil$ iterations, we can obtain all the Q_x bits of vector x . In every loop, the matrix A participates in a VMM computation. This VMM is also carried out by the INV crossbars storing A . We only need to connect these INV crossbars to the DAC/ADC interface and the crossbars are able to calculate VMM.

3) *Taylor Expansion for matrix A* . For matrix A , we cannot directly split it into multiple slices according to R_c . This is because there is no distributive law on A : $x = (A_1 + A_2)^{-1} \cdot b \neq A_1^{-1} \cdot b + A_2^{-1} \cdot b$. Therefore, we choose another route to address the problem and propose a method based on Taylor Expansion. We split the matrix A into two slices: the first $k \cdot R_c$ bits A_H , and the rest $Q_A - k \cdot R_c$ bits $A_L = (A - A_H) \cdot 2^{k \cdot R_c}$. A_H is written into the INV crossbars and A_L is written into a separate VMM crossbar as shown in Fig. 5. In the second-order training algorithms, A is a symmetric matrix [35]. Therefore, both A_H and A_L are also symmetric metrics and the matrix multiplication is commutative. We can simplify the differential of matrix A_H as:

$$d(A_H^{-1}) = -A_H^{-1} \cdot dA_H \cdot A_H^{-1} = -A_H^{-2} \cdot dA_H \quad (7)$$

According to Taylor Expansion, we have:

$$A^{-1} \cdot b = (A_H + A_L \cdot 2^{-k R_c})^{-1} \cdot b \quad (8)$$

$$= A_H^{-1} \cdot (I - P + P^2 - \dots) \cdot b \quad (9)$$

where $P = A_H^{-1} \cdot A_L \cdot 2^{-k R_c}$. In theory, we can obtain an accurate final result by computing all the terms on the right-hand side of Eqn. 9. In reality, we only need to compute a small number of terms in order to get the desired precision. Suppose the l^{th} term is $b_l = A_H^{-1} (-P)^l b$. Note that adding one more term only requires one more multiplication with P , i.e. $b_{l+1} = -P \cdot b_l$, which is essential to loop on the INV crossbars one more time (for $\cdot A_H^{-1}$), and one more time on the VMM crossbars (for $\cdot A_L$).

Pseudo-code of combining three steps into one complete high-precision matrix inversion is summarized in Fig. 4 (a).

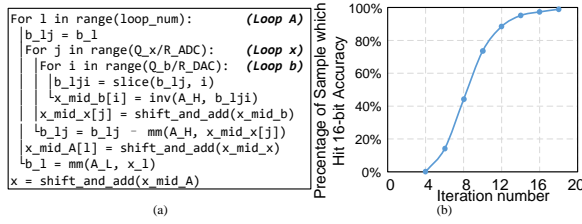


Fig. 4. (a) Pseudo-code of high-precision matrix inversion algorithm based on low-precision matrix inversion operation. (b) The number of Taylor expansion iteration required to achieve 16-bit accuracy in matrix inversion. The matrix's size is 1024×1024 . Matrix, input vector and result are all 16-bit quantized.

The three nested loops, *Loop b*, *Loop x* and *Loop A* correspond to the bit split of b , x and A . To better demonstrate the implementation of the three schemes described with Eqn. 6 and 9, we give an example in Fig. 5. Input vector b and result vector x are 4-bit quantized. The matrix A is 8-bit quantized and split into two 4-bit slices A_H , A_L . A_H is programmed to an INV crossbar and A_L is written to a VMM crossbar. Both ADC and DAC are 2-bit, therefore, both *Loop b* and *Loop x* have two iterations. Fig. 5(a) shows *Loop b* when $l = 0, j = 0$. The input 4-bit vector $b_{0,0}$ is split into two 2-bit slices $b_{0,0,0}$ and $b_{0,0,1}$ according to Eqn. 6. The two slices are successively input to the INV crossbar and the results are accumulated with S+A circuit. Fig. 5(b) shows *Loop x* when $l = 0$. In loop 0, we first compute the matrix inversion with 4-bit vector $b_{0,0} = b_0$ and A_H , and obtain 2-bit result $x_{mid_x}[0]$. After that, we input $x_{mid_x}[0]$ to the VMM crossbar and compute with A_H . Result of the VMM is subtracted from $b_{0,0}$ and obtain the input of the next loop $b_{0,1}$. The results of two iterations $x_{mid_x}[0,1]$ are accumulated with S+A circuit to obtain a 4-bit result. Fig. 5(c) shows the outside *Loop A*. In the first loop, we first compute the matrix inversion between the origin 4-bit vector $b_0 = b$ and A_H , and obtain the result $x_{mid_A}[0]$. $x_{mid_A}[0]$ is correspond to the first term in Eqn. (9) ($A_H^{-1}b$), therefore, it is added with the accumulated result by S+A. Then, $x_{mid_A}[0]$ is input to A_L and obtain the input of next loop b_1 . In the second loop, the intermediate result $x_{mid_A}[1]$ corresponds to the second term of Eqn.(9) ($A_H^{-1}Pb$). Therefore, it is subtracted from the accumulated result. After two loops, the result of VMM b_2 is a zero vector. This means that the accumulated result will not change in the following loops and the accurate 4-bit result is achieved.

Then we present the computing cycle spent on one high-precision matrix inversion. *Loop b* has $\lceil Q_b/R_{DAC} \rceil$ matrix inversion computations. *Loop x* has $\lceil Q_x/R_{ADC} \rceil$ loops and each loop contains one *Loop b* and one VMM computation. Each loop of *Loop A* contains one *Loop x* and one VMM computation. Suppose *Loop A* has N loops, the total cycles spent on one high-precision matrix inversion is:

$$c_{INV} = N \left(2 \left\lceil \frac{Q_b}{R_{DAC}} \right\rceil \cdot \left\lceil \frac{Q_x}{R_{ADC}} \right\rceil + \left\lceil \frac{Q_x}{R_{DAC}} \right\rceil \right) \quad (10)$$

Unlike the bit-slicing scheme for x and b , the iteration number for computing A is not decided by hardware parameters. This is because the convergence of Taylor Expansion is related

to the matrix A itself. The Taylor Expansion method is efficient only if the following two conditions are satisfied: First, A_H^{-1} is closed to A^{-1} . Second, the Taylor Equation can converge fast. It can be proved that both conditions have a common sufficient condition, which is that A 's condition number $\kappa(A)$ need to be small [33]. Fortunately, in the second-order optimization algorithms, Tikhonov regularization has been introduced to the SOI matrices [24], [31], [49]. This method can largely reduce the condition number of the matrix A and makes the Taylor Equation converge faster.

B. Verification of the Proposed High-Precision Matrix Inversion

To confirm the correctness of our proposed high-precision matrix-inversion, we write a RTL model with Verilog HDL for the circuit proposed in Fig. 2. As the ReRAM crossbar can not be directly modeled with Verilog, we write behavioral models for the low-precision INV and VMM crossbars with 4-bit precision and integrate them into the Verilog code. The non-idealism of OpAmp, including limited input resistance, output resistance and gain, is compensated with the method proposed in [14] and properly modeled.

We generate 10^6 input test vectors to verify the correctness of the proposed high-precision matrix inversion circuit in Verilog. The size of the input matrices is 1024×1024 . Tikhonov Normalization of the same level of ResNet 50 training is applied to the matrices. All the samples can achieve the required 16-bit accurate result after enough iterations. The relation between the percentage of samples that can achieve 16-bit accuracy and the loop number of *Loop A* is plotted in Fig. 4(b). Over 99% samples can achieve 16-bit accuracy within 18 loops. Therefore, in the following sections of the paper, we set the loop number of *Loop A* in Fig. 4 (b) to 18.

IV. ARCHITECTURE

Based on the high-precision matrix inversion presented in Section III, we propose RePAST, a ReRAM-based accelerator architecture for the second-order training. RePAST is composed of multiple tiles connected through an on-chip network. The structure of each tile is shown in Fig. 6. A tile contains a buffer, a bus for data movement, and several sub-tiles. In each sub-tile, there are one INV crossbar and several VMM crossbars for calculating matrix multiplication and inversion, as well as some other auxiliary circuits including input/output registers (IR/OR), activation function (Act), S+A and multipliers (Mul). The element-wise operations, including batch normalization and activation function, are processed by Acts, S+A and Muls. The ratio of VMM crossbars to INV crossbar in a sub-tile will be explained in Section VI-B. All the INV crossbars in one tile are connected by wires & switches. The connection is described in Section IV-A. The data communication between INV and VMM crossbars is through internal registers or eDRAM buffers.

We have summarized that there are two major operators in the second-order training algorithms: matrix multiplication

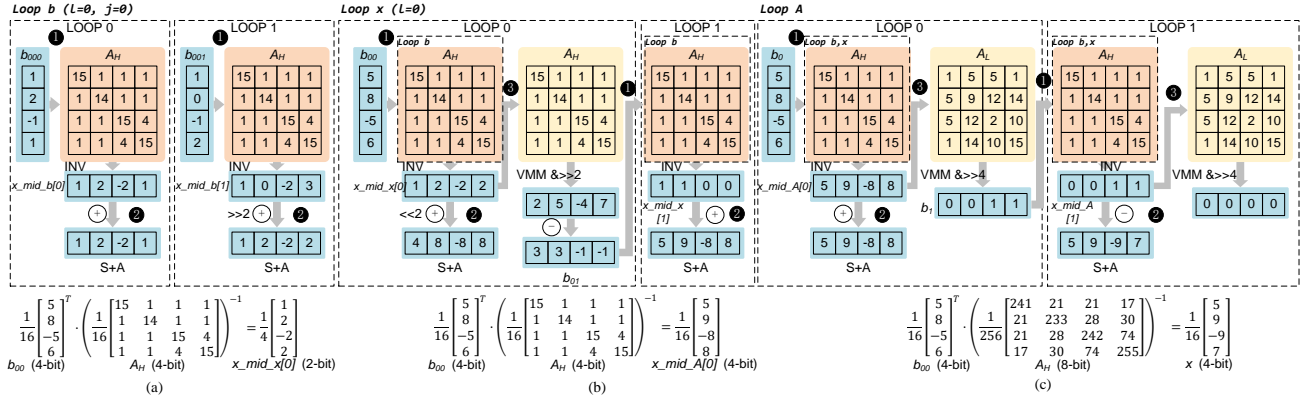


Fig. 5. An example of high-precision matrix inversion algorithm on ReRAM crossbar. (a) *Loop b* when $l = j = 0$. (b) *loop x* when $l = 0$. (c) *loop A*. Matrix A is 8-bit, input b and result x are 4-bit. DAC and ADC resolution is 2-bit. ReRAM cell can write 4-bit.

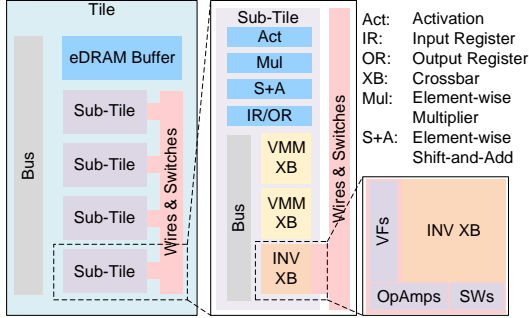


Fig. 6. Architecture overview of RePAST.

(MM) and INV. The VMM crossbars in a sub-tile will be responsible for the computation of MM. The INV operation is jointly handled by VMM and INV crossbars through multiple computing loops as the scheme proposed in Section III.

A. Connecting Multiple INV Crossbars

In the second-order training, the SOI matrix is usually larger than the size of a single INV crossbar. For example, one of VGG-19 layers has 512 input channels and the kernel size is 3×3 . When training this network with K-FAC algorithm, the SOI matrix A of this layer is 4608×4608 . But the typical size of a ReRAM crossbar is 256×256 , which is smaller than the SOI matrix. The VMM operation in high-precision matrix inversion can be performed by splitting the matrix to multiple VMM crossbars and adding up the mid-summations with digital adders [9]. While for the INV operation, the INV crossbars can only compute as one analog circuit. Therefore, we need to connect multiple INV crossbars so as to form a combined structure for large matrix inversion computation. Moreover, as the size of SOI matrix can be different over different networks, reconfigurability is required to change the connections.

The connection scheme for INV crossbars in a tile is depicted in Fig. 7(a). Around each INV crossbar, there is a group of VFs ①, a group of OpAmps ② and a group of switches (SWs) ③. The VFs are connected to the wordlines of the INV crossbar and can be configured to receive the analog signals from the left crossbar or from the OpAmps as inputs. SWs are connected to the bitlines of the INV crossbar. SWs and OpAmps are connected by a group of wires. If SWs and

OpAmps in the same INV crossbar are configured to connect, the analog signals from the crossbar's bitlines can be applied to the OpAmps as inputs.

We use an example to explain how to configure the connections for computing a large-size matrix inversion. Suppose matrix A 's size is 512×512 and the INV crossbar size is only 256×256 . This means that the matrix needs to occupy 2×2 INV crossbars. The configuration is shown in Fig. 7(b). The VFs of crossbar ② and ④ are configured to accept the signals from crossbar ① and ③, respectively. This makes crossbar ① and ② (or ③ and ④) share the same analog voltage input. The bitlines of crossbar ① and ③ are connected (shorted) by configuring their SWs and fed to the inputs of OpAmps in crossbar ③. This means that the current from bitlines in crossbar ① and ③ are accumulated and fed back to the wordlines of crossbar ③. Similarly, the bitlines of crossbar ② and ④, and the inputs of OpAmps in crossbar ① are connected, effectively forming an enlarged INV crossbar circuit structure. The input vector b can be applied to the DACs of INV crossbar ① and ②, and the results x are generated in the ADCs of crossbar ① and ③ as shown in the equivalent circuitry in Fig. 7(b). Therefore, the four crossbars are combined to function as one 512×512 matrix inversion circuit.

The maximum size of matrix inversion is limited by the total number of INV crossbars in a tile, which is an important architectural design parameter. Nevertheless, most second-order training algorithms allow us to flexibly tune the SOI matrix size to achieve different trade-offs between accuracy and cost. So we can always use the proper SOI matrix sizes to fulfill the limitation of INV crossbars, meanwhile keeping convergence rate in check.

B. Fused Operation

The circuit organization described in Fig. 7(a) makes it capable of computing a fused operation of low-precision matrix inversion and its immediately leading low-precision matrix multiplication. Suppose we need to calculate a fused-matrix-multiplication-and-inversion $x = (A_1 \cdot A_2)^{-1}b$, in which A_1 has a size of 512×256 and A_2 has a size of 256×512 . Therefore, both A_1 and A_2 occupy two crossbars. The connection is depicted in Fig. 7(c). The four INV crossbars are divided

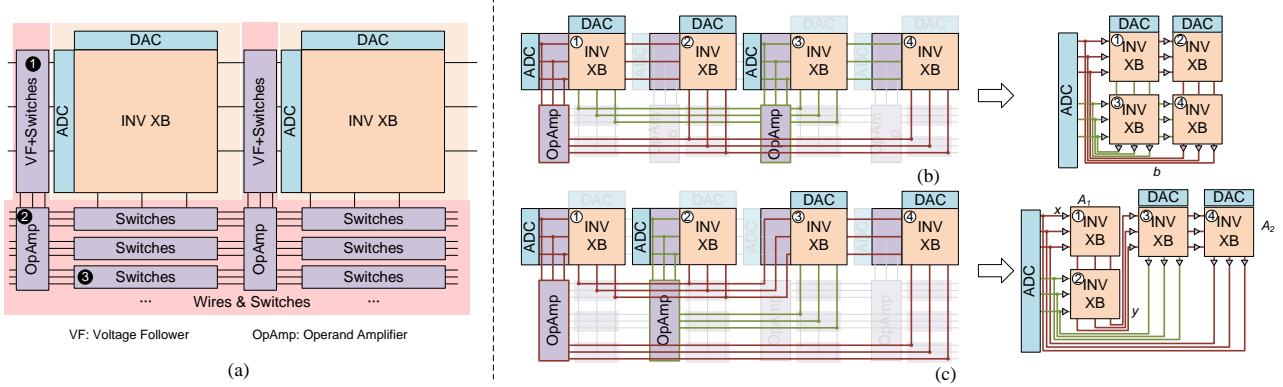


Fig. 7. The ReRAM crossbars for INV. (a) Multiple crossbars are in one sub-tile and can be configured. (b) The connection configuration when computing a 2×2 larger INV, and the equivalent circuit. (c) The connection configuration when fusing a VMM and an INV, and the equivalent circuit.

into 2 groups. Matrix A_1 is mapped to crossbar ① and ②, and matrix A_2 is mapped to crossbar ③ and ④. The bitlines of crossbar ① and ② are connected so that their currents are accumulated. The accumulated currents are applied to the wordlines of crossbar ③. The VFs of crossbar ④ is configured to share the same inputs with crossbar ③. The bitlines of crossbar ③ is connected to the inputs of OpAmps to feedback to the wordlines of crossbar ②. Similarly, the signals on the bitlines of crossbar ④ are fed back to the wordlines of crossbar ①. The equivalent circuitry is shown in Fig. 7(c). The analog signals (representing input x) on the wordlines of crossbar ① and ② are multiplied with the matrix A_1 , and the results on bitlines can be represented by $y = A_1 \cdot x$. The signal y is applied to the wordlines of crossbar ③ and ④, and the results are fed back to the input x . When we apply input b to the DACs in the crossbar ③ and ④, the relation between b and y is given by $b = A_2 \cdot y$. Since $y = A_1 \cdot x$, therefore, $b = A_1 \cdot A_2 \cdot x$, and in turn $x = (A_1 \cdot A_2)^{-1}b$. In this way, the circuit can carry out a low-precision fused-matrix-multiplication-and-inversion.

The high-precision matrix inversion scheme can also be applied to the fused operation. Suppose the matrix A_1 and A_2 are both 16-bit quantized. The higher 8 bits of A_1 is A_{1H} and $A_{1L} = (A_1 - A_{1H}) \cdot 2^8$. Similarly, the higher 8 bits of A_2 is A_{2H} and $A_{2L} = (A_2 - A_{2H}) \cdot 2^8$. Denote $A_H = A_{1H} \cdot A_{2H}$ and we have:

$$A_L = (A - A_H) \cdot 2^8 = (A_1 A_2 - A_{1H} A_{2H}) \cdot 2^8 \quad (11)$$

$$= A_{1H} A_{2L} + A_{1L} A_{2H} + A_{1L} A_{2L} \quad (12)$$

$$= A_1 \cdot A_{2L} + A_{1L} \cdot A_{2H} \quad (13)$$

According to Eqn. 9, A_H only participates in INV and A_L only participates in VMM. Therefore, A_{1H} and A_{2H} are programmed to the INV crossbars. A_1 , A_{1L} , A_{2H} and A_{2L} are programmed to the VMM crossbars. The matrix multiplication between input vector b and matrix A_L is computed via multiple VMMs according to Eqn. 13. Note that the two VMM terms can be computed in parallel, and each term contains two VMM operations (e.g. $A_1 \cdot A_{2L} \cdot b$). The total cycle is:

$$c_{INV+VMM} = N \left(2 \left\lceil \frac{Q_b}{R_{DAC}} \right\rceil \cdot \left\lceil \frac{Q_x}{R_{ADC}} \right\rceil + 2 \left\lceil \frac{Q_x}{R_{DAC}} \right\rceil \right) \quad (14)$$

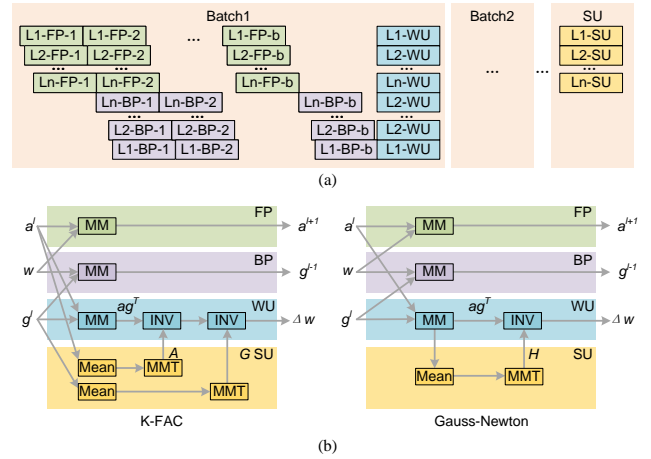


Fig. 8. (a) The pipeline of RePAST. 'L2-FP-1' represents the second layer's FP graph is executed on the first input. (b) The graph partition of two second-order training algorithms, K-FAC and Gauss-Newton. MM: Matrix Multiplication, MMT: Matrix Multiply with its Transpose

V. MAPPING SCHEME

A. Dataflow Graph (DFG) Partition

In the second-order training algorithms, the calculation of each DNN layer can be partitioned into four DFGs: Forward Propagation (FP), Backward Propagation (BP), Weight Update (WU), and SOI Update (SU). As shown in Fig. 8, for each batch, the FP graph is firstly executed on each input and obtain the error as output. During FP, the layers are calculated with inter-layer pipelining [41] to reduce latency. Whenever the FP on one input has been done, the BP graph starts. The WU graph only executes once after an entire batch has been processed. Δw values are computed and the weight matrices are updated. For every a few batches, the SU graph executes once to update the SOI matrices.

Take the two state-of-the-art second-order optimization methods, KFAC [31] and Gauss-Newton [24] as examples. In the FP graph, the input feature map a is multiplied with weight w to obtain the output feature map. In the BP graph, the error g is multiplied with weight w and back-propagated to the previous layer. In the WU graph, both of the two algorithms firstly compute the first-order gradient of weights. Then the gradients of weights multiply with the SOI matrix A , G , or

H to obtain the Δw . In the SU graph, the SOI matrices are updated with the rule described in Section II-A.

B. Pattern Mapping Scheme

We propose a mapping scheme for the two typical patterns in the SU graph to improve the performance of RePAST. The first is the MM-INV pattern, where the matrix for inversion is obtained after several matrix multiplication (MM) operators. The second pattern is composed of several successive MM or INV operators.

1) *MM-INV pattern*: This pattern can be frequently found in the SU graph of the two algorithms. The VMM operation is followed by a matrix inversion. Denote the matrix for inversion as $A \in \mathbb{R}^{m \times m}$, which is the product of matrix $a \in \mathbb{R}^{m \times n}$ and its transpose, $A = a \cdot a^T$. The matrix A 's inversion is multiplied with vector b to obtain the final result $x = (a \cdot a^T)^{-1} \cdot b$.

We can use two different strategies to map this pattern onto the crossbars, and they exhibit different crossbar occupations and computational costs with different matrix sizes. In the first strategy, $A = a \cdot a^T$ is calculated first using VMM crossbars and then mapped to INV crossbars to compute x . In the second strategy, A is not explicitly computed; instead, a and a^T are written to the INV crossbars to perform a fused-matrix-multiplication-and-inversion as described in Section IV-B.

Neither of the two strategies can always achieve the lowest crossbar occupation. In the first case, as shown in Fig. 9(a), where the size of matrix a is 1024×256 . The matrix A is the product of $a \cdot a^T$ so that its size will become 1024×1024 . Suppose the size of an INV crossbar is 256×256 . In the first strategy, A is mapped directly to the INV crossbars and occupies 16 INV crossbars. In the second strategy, either a or a^T occupies 4 INV crossbars, taking up a total of 8 INV crossbars. In comparison, the second strategy takes only half of the crossbars compared to the first one. As in Eqn. 14, the second strategy have a longer latency. However, the latency grows less than $2 \times$ compared to the first strategy but the overall performance is still better due to the much-reduced resource consumption.

In another case, as illustrated in Fig. 9(b), where the size of matrix a is 256×1024 so that the size of matrix A will be 256×256 and occupy only 1 INV crossbar. Therefore the first strategy should be more efficient since the second strategy will still need 8 crossbars.

With the observation above, we propose a smart mapping scheme for the MM-INV pattern. We can first locate an INV node in the DFG and then search backward. If the predecessor node is an MM, we need to decide whether to fuse the node with INV or not, by comparing a cost function of the two mapping strategies. Suppose the two matrices for MM is $m \times n$ and $n \times k$, and the size of an INV crossbar is $s \times s$. If we choose to fuse the nodes (the second strategy), the cost function is:

$$C_{fuse} = \alpha \cdot c_{VMM+INV} + \beta \left(\left\lceil \frac{n}{s} \right\rceil \cdot \left(\left\lceil \frac{m}{s} \right\rceil + \left\lceil \frac{k}{s} \right\rceil \right) \right) \quad (15)$$

The first term represents the computational latency for the fused-matrix-multiplication-and-inversion, and the second

term describes the condition of crossbar occupation. α and β are two empirical coefficients to trade off performance and resource consumption. Similarly, if we do not fuse the nodes (the first strategy), the cost function becomes:

$$C_{non-fuse} = \alpha \cdot c_{INV} + \beta \left(\left\lceil \frac{m}{s} \right\rceil \cdot \left\lceil \frac{k}{s} \right\rceil \right) \quad (16)$$

By simply comparing the two cost functions, we can decide which strategy should be adopted.

2) *Successive MM/INV pattern*: Different from the SU graph, the WU phase exhibits a different pattern. Take the WU graph of the K-FAC algorithm as an example. The weight update is calculated as $\Delta w = A^{-1} \cdot (a \cdot g^T) \cdot G^{-1}$. Consider a convolution layer with input channel, output channel, input feature map size and kernel size as c_{in} , c_{out} , $h \times w$ and $k \times k$. $A \in \mathbb{R}^{c_{in}k^2 \times c_{in}k^2}$, $G \in \mathbb{R}^{c_{out} \times c_{out}}$, $a \in \mathbb{R}^{c_{in}k^2 \times hw}$ and $g \in \mathbb{R}^{c_{out} \times hw}$. We also have two strategies to compute the formula. In the first strategy, we firstly compute $p = a \cdot g^T$ using VMM crossbars. As input feature map a is generated in FP phase and afterwards, the g is computed in BP phase. When waiting for g , we can program a to VMM crossbars. If a is larger than the size of a VMM crossbar, a is mapped to multiple crossbars with the splitting scheme in [9] and these crossbars can be programmed in parallel. Therefore, the crossbar programming latency can be completely covered by the FP and BP phase. After g is generated, we send g row by row to the crossbars, and this computation consumes $c_{out} \cdot c_{VMM}$ cycles. Then we compute $q = A^{-1} \cdot p$ by applying p row by row to the INV crossbars that store A . As $p \in \mathbb{R}^{c_{in}k^2 \times c_{out}}$, this procedure needs $c_{out} \cdot c_{INV}$ cycles. Finally, $\Delta w = q \cdot G^{-1}$ is computed by applying q row by row to the INV crossbars that store G , which takes $c_{in}k^2 \cdot c_{INV}$ cycles. As the first step and the second step can be performed in a pipeline, this strategy totally consumes $(c_{in}k^2 + c_{out}) \cdot c_{INV} + c_{VMM}$ cycles.

In the second strategy, we firstly compute $r = A^{-1} \cdot a$ by input a to the INV crossbars that store A , and write r to VMM crossbars. This computation can be executed immediately when a is generated in FP phase, and the latency can be covered because it will take a while for g to come back in the BP phase. Then we compute $s = g^T \cdot G^{-1}$ by input g to the INV crossbars that store G , which needs $hw \cdot c_{INV}$ cycles. Finally, $\Delta w = r \cdot s$ is computed by input s to the VMM crossbars that store r , and takes $c_{out} \cdot c_{VMM}$ cycles. This strategy needs $hw \cdot c_{INV} + c_{out} \cdot c_{VMM}$ cycles in total.

The two strategies are only different in computing latency, therefore, the cost functions of the two strategies are defined as the computing latency. For each layer, we compute the cost function of the two strategies and choose a faster strategy. In typical CNNs, for the first a few layers, the feature map size is usually large while the number of input or output channels is small. Therefore, the first strategy may spend fewer cycles to achieve a better performance. For the other layers, the feature map size becomes smaller with an increasing number of input and output channels, and the second strategy should be the better choice with reduced execution latency.

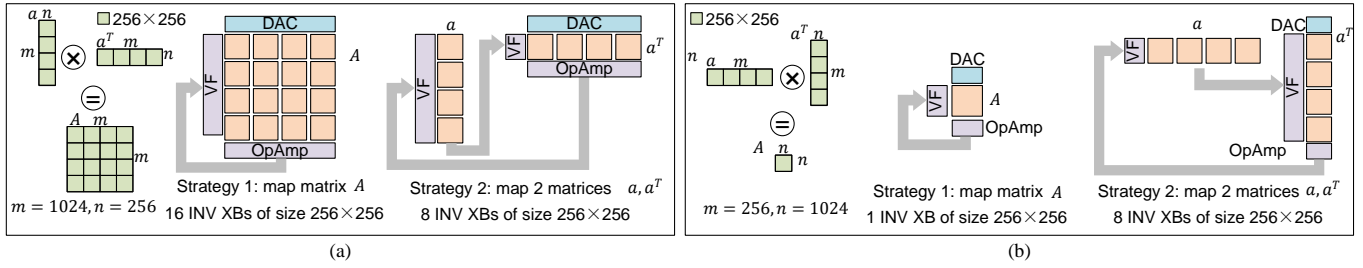


Fig. 9. Two cases when mapping the SU graph. The inversion of matrix A is needed and A is obtained by $A = a \cdot a^T$ (a) When $m \gg n$, strategy 2 can achieve a smaller crossbar occupation. (b) When $m \ll n$, strategy 1 is better.

TABLE I

MIN/MAX SOI MATRIX SIZE OF DNN BENCHMARKS. CONVOLUTION LAYERS ARE FORMATTED AS $Ck \times k, c_{in}/c_{out}$. SOI MATRIX SIZE $bB+r$ MEANS b BLOCKS OF SIZE 1024×1024 AND ONE BLOCK OF SIZE $r \times r$

Network		Layer	SOI Matrix
VGG-13/16/19	Min	C3x3, 3/64	A: 0B+27, G: 0B+64
	Max	C3x3, 512/512	A: 4B+512, G: 0B+512
MSRA-1/2	Min	C7x7, 3/96	A: 0B+147, G: 0B+96
	Max	C3x3, 512/512	A: 4B+512, G: 0B+512
ResNet-50/101	Min	C1x1, 64/64	A: 0B+64, G: 0B+64
	Max	C3x3, 512/2048	A: 4B+512, G: 0B+512
Bert	Min	Projection	A: 0B+768, G: 0B+64
	Max	Feed Forward	A: 3B+0, G: 0B+768

VI. EVALUATION

A. Experiment setup

We evaluate our proposed RePAST with seven large-scale CNNs (VGG-13, VGG-16 and VGG-19 [43], MSRA-1 and MSRA-2 [16], ResNet-50 and ResNet-101 [17]) on ImageNet dataset [11], BERT [12] on MLPerf dataset [32], and auto-encoder [19] on MINST dataset [27]. The batch size is set to 256, and the SOI matrices are updated after every 10 batches. We present the minimum and maximum SOI matrix sizes in TABLE I.

We compare the RePAST architecture with NVidia Tesla V100 GPU and one recent PIM architecture for the first-order training, PipeLayer [44]. Second-order training algorithm K-FAC [31] is executed on GPU and RePAST and SGD is executed on GPU and Pipelayer. To evaluate the energy consumption and latency of GPU, we train the benchmarks with Mindspore framework [34]. We build a cycle-accurate simulator to evaluate RePAST's area and energy consumption. We adopt the ReRAM crossbar energy/area model in [21], ADC energy/area model in [26], and DAC energy/area model in [40]. The resolution of ADC and DAC is 8-bit and 4-bit respectively. The OpAmp energy/area model is from [37]. The eDRAM buffer and bus are simulated with CACTI7.0 [2]. Hyper Transport link for inter-chip communication use the model from [41]. All the circuits are scaled to 28nm technology. To make a fair comparison with PipeLayer, we use the same model for the common circuits of the two architectures, such as ReRAM crossbars. The RePAST tiles' computation and memory access are controlled by a state machine. We write a simple optimizer to generate the state machine according to the DNN's hyper-parameters. Energy

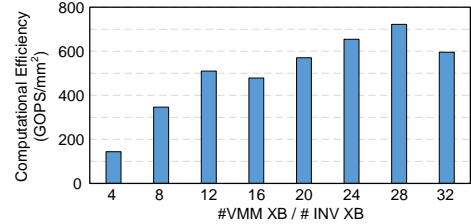


Fig. 10. Design space exploration. We search for the best proportion between VMM and INV crossbar number with average computational efficiency across benchmarks as metric.

consumption of GPU is evaluated with `nvidia-smi` tool. The ReRAM crossbar size in RePAST is set to 256×256 and each ReRAM cell can support 4-bit precision. We always assign one INV crossbar in a sub-tile. In order to support a wider range of block size in the second-order training algorithms, we set the total number of INV crossbars (or sub-tiles) in a tile as 16 so that a maximum block size of 1024×1024 can be supported. This block size is larger than most layer's SOI matrices and these matrices are not approximated in the algorithm. For example, over 80% of ResNet-50's SOI matrix is smaller than this size. Hyper-parameters of the mapping scheme are set to $\alpha = 1$ and $\beta = 0.1$.

Cycle Time. We set the cycle time of RePAST's ReRAM crossbars as 100 ns. This value is commonly used in ReRAM-based accelerators [5], [28], [41] because it is coherence to current ADC frequency. For INV crossbars, the settling time is proportion to the λ_{min}^{-1} of matrix, and OpAMP parameters $L_0^{-1}\omega_0^{-1}$, and is independent to the size of Matrix size. [14]'s INV crossbar can settle down within 50 ns. We use the same OpAMP as [14], and the Tikhonov normalization in second-order training can reduce the λ_{min}^{-1} value of matrix. Therefore, our INV corssbar can settle down within 100 ns.

B. Design Space Exploration

One important design parameter of the RePAST architecture is the proportion between the INV crossbar number and the VMM crossbar number in a tile. On the one hand, if there are more INV crossbars and fewer VMM crossbars in the architecture, the latency of FP and BP graph can be longer because they are mainly composed of vector-matrix multiplication operations. Otherwise, the WU graph, which is mainly composed of matrix inversion, needs more time to compute

TABLE II
REPAST'S AREA BREAKDOWN (IN mm^2).

Component	Spec	Area	Component	Spec	Area
VMM XB			INV XB		
ADC	Resolution: 8 Freq: 1.2GSps Num: 256	0.00236	ADC	Resolution: 8 Freq: 1.2GSps Num: 256	0.00236
DAC	Resolution: 4 Num: 256	0.00068	DAC	Resolution: 4 Num: 256	0.00068
ReRAM	Size: 256 Num: 1	0.0001	ReRAM	Size: 256 Num: 3	0.0003
			OpAmp	Num: 512	0.0128
Total	Num: 28	0.0879	Total	Num: 1	0.0161
Sub-Tile					
IR	Size: 4kB	0.004	OR	Size: 1kB	0.002
Act	Num: 1	0.0006	S+A	Num: 29	0.00174
Mul	Num: 1	0.0006			
			Total	Num: 16	1.80
Tile					
eDRAM	Size: 512kB	0.898	Bus	Num: 928	0.218
			Total	Num: 22	64.2
Hyper Tr.		22.9			
			Chip Total		87.1

and may also reduce the throughput. We conduct a design space exploration on this parameter to obtain the optimal architectural configuration. As different neural networks have different layer sizes, the optimal architectural configuration can be different. We use the averaged computational efficiency across all the benchmarks as a metric. The result is shown in Fig. 10. The metrics increase when the proportion of VMM and INV crossbar grows. The anomalous trends between the #VMM XB / #INV XB value 12 and 16 is because the buffer area grows non-uniformly when the buffer size grows. When #VMM XB / #INV XB is larger than 32, the INV crossbar number is not large enough to arrange large NNs, e.g., VGG-19. The best computational efficiency ($722.1\text{GOPS}/mm^2$) is achieved when there are 28 VMM crossbars in each sub-tile, or $28 \times 16 = 448$ VMM crossbars in each tile containing 16 INV crossbars.

With the results of design space exploration, the configuration of RePAST is decided. The eDRAM buffer of each tile is set to 512kB and the bus width is 256 bits. With the inter-layer pipeline proposed in [41], this buffer size is enough to store the intermediate results. Note that we clock the eDRAM at 1GHz while the crossbars are running at 10MHz, so that the eDRAM bandwidth should be enough for inner-tile data transfers. The area of one RePAST chip is $87.1mm^2$, including 22 tiles with 16 INV and 448 VMM crossbars per tile. This chip area is close to PipeLayer's [44]. Area breakdown is presented in TABLE II. In the following experiments, we use 8 chips for both PipeLayer and RePAST to train the benchmarks, so that the total area is close to the area of a single Tesla V100 GPU ($815mm^2$). For smaller networks that can not occupy all the ReRAM crossbars in the 8 chips, we duplicate the matrices stored in ReRAM crossbars to speed up the training.

C. Speedup and Energy Saving

We compare the performance of RePAST, GPU and PipeLayer in Fig. 11. For each benchmark, we report the training time of the first-order training on GPU ($GPU - 1^{st}$) and PipeLayer, and the second-order training on GPU

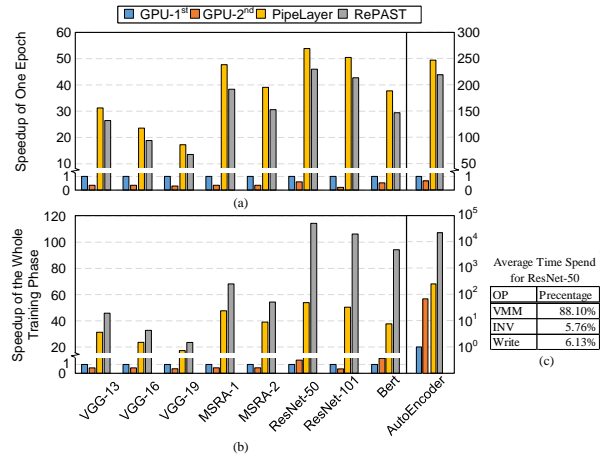


Fig. 11. (a) (b) Speedup of RePAST compared to GPU and PipeLayer over neural network benchmarks. All the values are normalized to GPU-1st. Autoencoder use the secondary Y axis. (c) Average Time Spend on the operations when training ResNet-50

($GPU - 2^{nd}$) and RePAST. The block size of the second-order training algorithm is set to 1024. Fig. 11 (a) depicts the training time of one epoch and Fig. 11 (b) depicts the total training time. For CNNs, we regard that the training is finished when the accuracy reaches within 0.5% lower than the standard accuracy. Compared to $GPU - 2^{nd}$, RePAST can achieve an average of $115.8\times$ reduction in training time across the benchmarks. Compared to the first-order training on PipeLayer, RePAST needs 21.5% longer training time for each epoch on average. However, thanks to the faster convergence rate in the second-order training which means much fewer epochs are needed for the entire training process, the total training time of RePAST is $11.4\times$ shorter than PipeLayer. In contrast, if only using GPUs, the second-order algorithm brings an average of 58.8% more training time compared to the first-order algorithm in GPU because the SOI inversion computation on GPU is too slow and may completely over-ride the benefit of fast convergence in the second-order algorithm. For VGG-13/16/19, MSRA-1/2 and ResNet-101, the fast convergence rate cannot compensate for the inversion overhead on GPU. For small-scale autoencoder, RePAST's per-epoch training time is 12.7% longer than PipeLayer. Nevertheless, the convergence of second-order training on autoencoder is $109\times$ faster than first-order training [31]. This results in a $88.7\times$ shorter training time compared to PipeLayer.

Time Spend breakdown on the three operations when training ResNet-50 listed in Fig. 11 (c). Note that vector-matrix multiplication and matrix inversion are actually computed in parallel with different crossbars. The time spend percentage is averaged number among the crossbars. Matrix inversion and writing only account for 11.9% of crossbar's computing time because they only happens after every several batches.

The energy saving of RePAST over GPU and PipeLayer is shown in Fig. 12. RePAST can achieve an average energy saving of $41.9\times$ and $12.8\times$ compared to GPU and PipeLayer respectively.

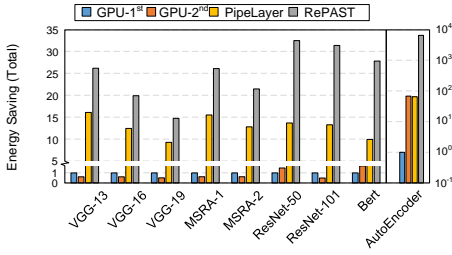


Fig. 12. Energy consumption of RePast compared to GPU and PipeLayer over neural network benchmarks. All the values are normalized to GPU-1st.

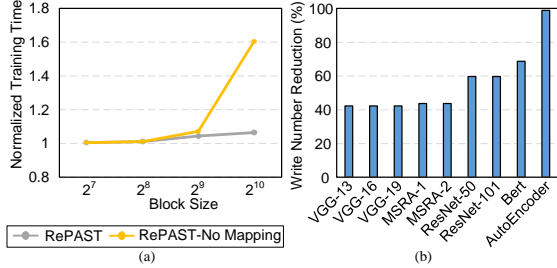


Fig. 13. (a) Training time of RePast with/without mapping scheme over different block size. Normalized to the value on block size 128 of RePast with mapping scheme. (b) Write number reduction of RePast compared to PipeLayer.

D. Write Number

Fig. 13 (b) shows that RePast can reduce 55.7% write number on average during the whole training phase compared to PipeLayer. As with first-order training, weights on VMM crossbars are updated after each batch. SOI on INV crossbars are updated after several batches. Note that the matrices on INV crossbars keep unchanged during matrix inversion computing. Therefore, RePast’s write frequency is no higher than Pipelayers. Thanks to the fast convergence of second-order training, the iteration number of the whole training phase is reduced. This significantly reduce the writes and improve the endurance of RePast.

E. Impact of the Mapping Scheme

We evaluate the epoch training time of ResNet-50 on-RePast with different block size and plot the results in Fig. 13 (a) to study the impact of mapping schemes. RePast-No Mapping denotes that the original dataflow is directly mapped to the RePast without using the mapping schemes proposed in Section V-B. When the block size is smaller than the crossbar size of 256, the two series have the same training time. This is because the small blocks in SOI matrices can not even occupy a single INV crossbar. The first strategy of MM-INV pattern will always achieve the best saving. When the block size becomes larger, the training latency of RePast-No Mapping increases sharply. This is because the crossbar occupation of SOI blocks increases squarely to the block size. While with our proposed mapping schemes, the training latency increases more gently with a more flat slope.

We can illustrate that there is a maximum crossbar occupation of SOI matrices with the increasing of block sizes if we perform the mapping scheme for K-FAC algorithm. Suppose the crossbar size is s . The FIM for inversion A is obtained

by $A = a \cdot a^T$, and $A \in R^{c_{in}k^2 \times c_{in}k^2}$, $a \in R^{c_{in}k^2 \times hw}$. The matrix A is approximated by diagonal block matrix with block size B , with a total of $\lceil c_{in}k^2/B \rceil$ blocks. Suppose the i^{th} block $A_i = A[iB : (i+1)B, iB : (i+1)B]$. A_i is computed by $a_i \cdot a_i^T$, where $a_i = a[iB : (i+1)B, :] \in R^{B \times hw}$. For each block A_i , we can perform the mapping scheme, and the crossbar number is $\min\left(\left(\frac{B}{s}\right)^2, 2\frac{hw}{s} \cdot \frac{B}{s}\right)$. When the

block size B is large ($B > 2hw$), this value will becomes $2hwB/s^2$. For the whole matrix A , the crossbar number is $2hwB/s^2 \cdot c_{in}k^2/B = 2hwc_{in}k^2/s^2$, which is a constant independent to the block size B . Therefore, the block size will not influence the resource occupation of RePast with our mapping schemes. Note that the conclusion is suitable for convolution layer of any size. We only need to instantiate the above parameters c_{in}, hw, s, k into the real convolution layer’s size. This conclusion is meaningful because RePast is friendly to large block size and larger block size can take better advantage of the higher convergence rate in the second-order training algorithms.

VII. RELATED WORK

ReRAM-based Accelerators. [9], [41], [50] design ReRAM-based accelerators for DNN inference. Some studies improve the energy efficiency of ReRAM-based DNN accelerator [5], [10], [28], [39]. [8], [44] extend the ReRAM-based accelerator to the first-order training for DNNs. The main problem of ReRAM-based accelerators for DNN training is limited endurance of ReRAM. [4] improve the endurance of ReRAM-based accelerator by swapping the rows during DNN training. [52] propose a weight-skewed training and aging-aware mapping. Another problem is the non-ideality in ReRAM’s analog computation. [3], [42] propose methods to tolerant the thermal noise. [6], [29] add the hardware non-ideality to the loss function and retrain the DNN. [18] design a end-to-end framework to adapt the non-ideality. [25], [46] propose to use unary coding to reduce the impact of variance.

Second-Order Training Algorithm. Newton method and Natural Gradient method are two traditional second-order optimizing methods. The SOI’s size is heavy for most applications. The Quasi-Newton method [35], [54] uses the rank-1 matrices to approximate the Hessian matrix, but this size is still unacceptable for DNNs. To further reduce the storage of Hessian matrix in Newton method, approximate Hessian [22], [51] and Hessian-free methods [24], [49] are proposed. [1], [15], [30], [31] approximate the FIM in Natural Gradient method. SOI change slowly during training. Therefore, [7], [36] use the outdated SOI to reduce the update frequency.

VIII. CONCLUSION

In this work, we propose RePast, a ReRAM-based PIM accelerator for the second-order training of DNN. We propose a novel high-precision matrix-inversion algorithm and implementation with normal VMM and INV crossbars. The INV crossbar in RePast is connected with analog wires and can support a fused operation of low-precision matrix

inversion and its immediately leading low-precision matrix multiplication. Based on this feature, we propose a mapping scheme for MM-INV and successive MM/INV pattern in the algorithms. Results show that RePAST can achieve an average of $115.8 \times / 11.4 \times$ speedup and $41.9 \times / 12.8 \times$ energy saving compared to a GPU counterpart and PipeLayer on large-scale DNNs. Moreover, the RePAST is not sensitive to the second-order information and can better take advantage of the high convergence rate of the second-order training algorithms.

REFERENCES

- [1] R. Anil, V. Gupta, T. Koren, K. Regan, and Y. Singer, "Second order optimization made practical," *CoRR*, vol. abs/2002.09018, 2020. [Online]. Available: <https://arxiv.org/abs/2002.09018>
- [2] R. Balasubramonian, A. B. Kahng, N. Muralimanohar, A. Shafiee, and V. Srinivas, "Cacti 7: New tools for interconnect exploration in innovative off-chip memories," *ACM Trans. Archit. Code Optim.*, vol. 14, no. 2, Jun. 2017. [Online]. Available: <https://doi.org/10.1145/3085572>
- [3] M. V. Beigi and G. Memik, "Thermal-aware optimizations of rram-based neuromorphic computing systems," in *Proceedings of the 55th Annual Design Automation Conference*, ser. DAC '18. New York, NY, USA: Association for Computing Machinery, 2018. [Online]. Available: <https://doi.org/10.1145/3195970.3196128>
- [4] Y. Cai, Y. Lin, L. Xia, X. Chen, S. Han, Y. Wang, and H. Yang, "Long live time: Improving lifetime for training-in-memory engines by structured gradient sparsification," in *2018 55th ACM/ESDA/IEEE Design Automation Conference (DAC)*, June 2018, pp. 1–6.
- [5] W. Cao, Y. Zhao, A. Bolor, Y. Han, X. Zhang, and L. Jiang, "Neural-pim: Efficient processing-in-memory with neural approximation of peripheral," *IEEE Transactions on Computers*, pp. 1–1, 2021.
- [6] L. Chen, J. Li, Y. Chen, Q. Deng, J. Shen, X. Liang, and L. Jiang, "Accelerator-friendly neural-network training: Learning variations and defects in rram crossbar," in *Design, Automation & Test in Europe Conference & Exhibition (DATE)*, 2017, March 2017, pp. 19–24.
- [7] M. Chen, K. Gao, X. Liu, Z. Wang, N. Ni, Q. Zhang, L. Chen, C. Ding, Z. Huang, M. Wang, S. Wang, F. Yu, X. Zhao, and D. Xu, "Thor, trace-based hardware-driven layer-oriented natural gradient descent computation," *Proceedings of the AAI Conference on Artificial Intelligence*, vol. 35, no. 8, pp. 7046–7054, May 2021. [Online]. Available: <https://ojs.aaai.org/index.php/AAAI/article/view/16867>
- [8] M. Cheng, L. Xia, Z. Zhu, Y. Cai, Y. Xie, Y. Wang, and H. Yang, "Time: A training-in-memory architecture for rram-based deep neural networks," *IEEE Transactions on Computer-Aided Design of Integrated Circuits and Systems*, vol. 38, no. 5, pp. 834–847, May 2019.
- [9] P. Chi, S. Li, C. Xu, T. Zhang, J. Zhao, Y. Liu, Y. Wang, and Y. Xie, "Prime: A novel processing-in-memory architecture for neural network computation in rram-based main memory," in *Proceedings of the 43rd International Symposium on Computer Architecture*, ser. ISCA '16. IEEE Press, 2016, p. 27–39. [Online]. Available: <https://doi.org/10.1109/ISCA.2016.13>
- [10] T. Chou, W. Tang, J. Botimer, and Z. Zhang, "Cascade: Connecting rams to extend analog dataflow in an end-to-end in-memory processing paradigm," in *Proceedings of the 52nd Annual IEEE/ACM International Symposium on Microarchitecture*, ser. MICRO '52. New York, NY, USA: Association for Computing Machinery, 2019, p. 114–125. [Online]. Available: <https://doi.org/10.1145/3352460.3358328>
- [11] J. Deng, W. Dong, R. Socher, L.-J. Li, K. Li, and L. Fei-Fei, "ImageNet: A Large-Scale Hierarchical Image Database," in *CVPR09*, 2009.
- [12] J. Devlin, M.-W. Chang, K. Lee, and K. Toutanova, "Bert: Pre-training of deep bidirectional transformers for language understanding," 2019.
- [13] J. Duchi, E. Hazan, and Y. Singer, "Adaptive subgradient methods for online learning and stochastic optimization," *J. Mach. Learn. Res.*, vol. 12, no. null, p. 2121–2159, Jul. 2011.
- [14] B. Feinberg, R. Wong, T. P. Xiao, C. H. Bennett, J. N. Rohan, E. G. Boman, M. J. Marinella, S. Agarwal, and E. Ipek, "An analog preconditioner for solving linear systems," in *2021 IEEE International Symposium on High-Performance Computer Architecture (HPCA)*, Feb 2021, pp. 761–774.
- [15] R. Grosse and J. Martens, "A kronecker-factored approximate fisher matrix for convolution layers," in *Proceedings of The 33rd International Conference on Machine Learning*, ser. Proceedings of Machine Learning Research, M. F. Balcan and K. Q. Weinberger, Eds., vol. 48. New York, New York, USA: PMLR, 20–22 Jun 2016, pp. 573–582. [Online]. Available: <http://proceedings.mlr.press/v48/grosse16.html>
- [16] K. He, X. Zhang, S. Ren, and J. Sun, "Delving deep into rectifiers: Surpassing human-level performance on imagenet classification," in *2015 IEEE International Conference on Computer Vision (ICCV)*, 2015, pp. 1026–1034.
- [17] K. He, X. Zhang, S. Ren, and J. Sun, "Deep residual learning for image recognition," 2015.
- [18] Z. He, J. Lin, R. Ewetz, J.-S. Yuan, and D. Fan, "Noise injection adaption: End-to-end rram crossbar non-ideal effect adaption for neural network mapping," in *Proceedings of the 56th Annual Design Automation Conference 2019*, ser. DAC '19. New York, NY, USA: Association for Computing Machinery, 2019. [Online]. Available: <https://doi.org/10.1145/3316781.3317870>
- [19] G. E. Hinton and R. R. Salakhutdinov, "Reducing the dimensionality of data with neural networks," *Science*, vol. 313, no. 5786, pp. 504–507, 2006. [Online]. Available: <https://www.science.org/doi/abs/10.1126/science.1127647>
- [20] X. Hong, D. J. Loy, P. A. Dananjaya, F. Tan, C. Ng, and W. Lew, "Oxide-based rram materials for neuromorphic computing," *J Mater Sci*, 2018.
- [21] M. Hu, J. P. Strachan, Z. Li, E. M. Grafals, N. Davila, C. Graves, S. Lam, N. Ge, J. J. Yang, and R. S. Williams, "Dot-product engine for neuromorphic computing: Programming 1T1m crossbar to accelerate matrix-vector multiplication," in *2016 53rd ACM/EDAC/IEEE Design Automation Conference (DAC)*, June 2016, pp. 1–6.
- [22] X. Huang, X. Liang, Z. Liu, L. Li, Y. Yu, and Y. Li, "Span: A stochastic projected approximate newton method," in *Proceedings of the AAAI Conference on Artificial Intelligence*, vol. 34, no. 02, 2020, pp. 1520–1527.
- [23] D. P. Kingma and J. Ba, "Adam: A method for stochastic optimization," 2014.
- [24] R. Kiros, "Training neural networks with stochastic hessian-free optimization," 2013.
- [25] A. Krizhevsky, I. Sutskever, and G. E. Hinton, "Imagenet classification with deep convolutional neural networks," *Commun. ACM*, vol. 60, no. 6, p. 84–90, May 2017. [Online]. Available: <https://doi.org/10.1145/3065386>
- [26] L. Kull, T. Toifl, M. Schmatz, P. A. Francesc, C. Menolfi, M. Brändli, M. Kossel, T. Morf, T. M. Andersen, and Y. Leblebici, "A 3.1 mw 8b 1.2 gs/s single-channel asynchronous sar adc with alternate comparators for enhanced speed in 32 nm digital soi cmos," *IEEE Journal of Solid-State Circuits*, vol. 48, no. 12, pp. 3049–3058, Dec 2013.
- [27] Y. LeCun, C. Cortes, and C. Burges, "Mnist handwritten digit database," *ATT Labs [Online]*. Available: <http://yann.lecun.com/exdb/mnist>, vol. 2, 2010.
- [28] W. Li, P. Xu, Y. Zhao, H. Li, Y. Xie, and Y. Lin, "Timely: Pushing data movements and interfaces in pim accelerators towards local and in time domain," in *2020 ACM/IEEE 47th Annual International Symposium on Computer Architecture (ISCA)*, Conference Proceedings, pp. 832–845.
- [29] B. Liu, H. Li, Y. Chen, X. Li, Q. Wu, and T. Huang, "Vortex: Variation-aware training for memristor x-bar," in *Proceedings of the 52nd Annual Design Automation Conference*, ser. DAC '15. New York, NY, USA: Association for Computing Machinery, 2015. [Online]. Available: <https://doi.org/10.1145/2744769.2744930>
- [30] J. Martens, J. Ba, and M. Johnson, "Kronecker-factored curvature approximations for recurrent neural networks," in *International Conference on Learning Representations*, 2018. [Online]. Available: <https://openreview.net/forum?id=HyMTkQZAb>
- [31] J. Martens and R. Grosse, "Optimizing neural networks with kronecker-factored approximate curvature," in *Proceedings of the 32nd International Conference on Machine Learning*, ser. Proceedings of Machine Learning Research, F. Bach and D. Blei, Eds., vol. 37. Lille, France: PMLR, 07–09 Jul 2015, pp. 2408–2417. [Online]. Available: <http://proceedings.mlr.press/v37/martens15.html>
- [32] P. Mattson, C. Cheng, C. Coleman, G. Damos, P. Micikevicius, D. Patterson, H. Tang, G.-Y. Wei, P. Bailis, V. Bittorf, D. Brooks, D. Chen, D. Dutta, U. Gupta, K. Hazelwood, A. Hock, X. Huang, A. Ike, B. Jia, D. Kang, D. Kanter, N. Kumar, J. Liao, G. Ma, D. Narayanan, T. Oguntebi, G. Pekhimenko, L. Pentecost, V. J. Reddi, T. Robie,

- T. S. John, T. Tabaru, C.-J. Wu, L. Xu, M. Yamazaki, C. Young, and M. Zaharia, "MLperf training benchmark," 2019.
- [33] C. D. Meyer, *Matrix analysis and applied linear algebra*. Siam, 2000, vol. 71.
- [34] Mindspore. Mindspore. [Online]. Available: <https://github.com/mindspore-ai/mindspore>
- [35] J. Nocedal and S. Wright, *Numerical optimization*. Springer Science & Business Media, 2006.
- [36] K. Osawa, Y. Tsuji, Y. Ueno, A. Naruse, C.-S. Foo, and R. Yokota, "Scalable and practical natural gradient for large-scale deep learning," 2020.
- [37] X. Peng, W. Sansen, L. Hou, J. Wang, and W. Wu, "Impedance adapting compensation for low-power multistage amplifiers," *IEEE Journal of Solid-State Circuits*, vol. 46, no. 2, pp. 445–451, 2011.
- [38] N. Qian, "On the momentum term in gradient descent learning algorithms," *Neural Networks*, vol. 12, no. 1, pp. 145–151, 1999. [Online]. Available: <https://www.sciencedirect.com/science/article/pii/S0893608098001166>
- [39] X. Qiao, X. Cao, H. Yang, L. Song, and H. Li, "Atomlayer: A universal reram-based cnn accelerator with atomic layer computation," in *2018 55th ACM/ESDA/IEEE Design Automation Conference (DAC)*, June 2018, pp. 1–6.
- [40] M. Saberli, R. Lotfi, K. Mafinezhad, and W. A. Serdijn, "Analysis of power consumption and linearity in capacitive digital-to-analog converters used in successive approximation adcs," *IEEE Transactions on Circuits and Systems I: Regular Papers*, vol. 58, no. 8, pp. 1736–1748, Aug 2011.
- [41] A. Shafiee, A. Nag, N. Muralimanohar, R. Balasubramonian, J. P. Strachan, M. Hu, R. S. Williams, and V. Srikumar, "Isaac: A convolutional neural network accelerator with in-situ analog arithmetic in crossbars," in *2016 ACM/IEEE 43rd Annual International Symposium on Computer Architecture (ISCA)*. IEEE, 2016, Conference Proceedings.
- [42] H. Shin, M. Kang, and L.-S. Kim, "A thermal-aware optimization framework for reram-based deep neural network acceleration," in *Proceedings of the 39th International Conference on Computer-Aided Design*, ser. ICCAD '20. New York, NY, USA: Association for Computing Machinery, 2020. [Online]. Available: <https://doi.org/10.1145/3400302.3415665>
- [43] K. Simonyan and A. Zisserman, "Very deep convolutional networks for large-scale image recognition," 2015.
- [44] L. Song, X. Qian, H. Li, and Y. Chen, "Pipelay: A pipelined reram-based accelerator for deep learning," in *2017 IEEE International Symposium on High Performance Computer Architecture (HPCA)*, Feb 2017, pp. 541–552.
- [45] T. Song, X. Chen, and Y. Han, "Eliminating iterations of iterative methods: Solving large-scale sparse linear system in \mathbb{F}_2 with rram-based in-memory accelerator," in *Proceedings of the 2021 on Great Lakes Symposium on VLSI*, ser. GLSVLSI '21. New York, NY, USA: Association for Computing Machinery, 2021, p. 71–76. [Online]. Available: <https://doi.org/10.1145/3453688.3461510>
- [46] Y. Sun, C. Ma, Z. Li, Y. Zhao, J. Jiang, W. Qian, R. Yang, Z. He, and L. Jiang, "Unary coding and variation-aware optimal mapping scheme for reliable reram-based neuromorphic computing," *IEEE Transactions on Computer-Aided Design of Integrated Circuits and Systems*, vol. 40, no. 12, pp. 2495–2507, Dec 2021.
- [47] Z. Sun, G. Pedretti, P. Mannocci, E. Ambrosi, A. Bricalli, and D. Ielmini, "Time complexity of in-memory solution of linear systems," *IEEE Transactions on Electron Devices*, vol. 67, no. 7, pp. 2945–2951, July 2020.
- [48] M. S. Q. Truong, E. Chen, D. Su, L. Shen, A. Glass, L. R. Carley, J. A. Bain, and S. Ghose, "Racer: Bit-pipelined processing using resistive memory," in *MICRO-54: 54th Annual IEEE/ACM International Symposium on Microarchitecture*, ser. MICRO '21. New York, NY, USA: Association for Computing Machinery, 2021, p. 100–116. [Online]. Available: <https://doi.org/10.1145/3466752.3480071>
- [49] C.-C. Wang, K. L. Tan, C.-T. Chen, Y.-H. Lin, S. S. Keerthi, D. Mahajan, S. Sundararajan, and C.-J. Lin, "Distributed newton methods for deep neural networks," *Neural Computation*, vol. 30, no. 6, pp. 1673–1724, June 2018.
- [50] X. Yang, B. Yan, H. Li, and Y. Chen, "Retransformer: Reram-based processing-in-memory architecture for transformer acceleration," in *Proceedings of the 39th International Conference on Computer-Aided Design*, ser. ICCAD '20. New York, NY, USA: Association for Computing Machinery, 2020. [Online]. Available: <https://doi.org/10.1145/3400302.3415640>
- [51] Z. Yao, A. Gholami, S. Shen, M. Mustafa, K. Keutzer, and M. W. Mahoney, "Adahessian: An adaptive second order optimizer for machine learning," 2021.
- [52] S. Zhang, G. L. Zhang, B. Li, H. H. Li, and U. Schlichtmann, "Aging-aware lifetime enhancement for memristor-based neuromorphic computing," in *2019 Design, Automation & Test in Europe Conference & Exhibition (DATE)*, March 2019, pp. 1751–1756.
- [53] Q. Zheng, X. Li, Z. Wang, G. Sun, Y. Cai, R. Huang, Y. Chen, and H. H. Li, "Mobilattice: A depth-wise dcnn accelerator with hybrid digital/analog nonvolatile processing-in-memory block," in *Proceedings of the 39th International Conference on Computer-Aided Design*, ser. ICCAD '20. New York, NY, USA: Association for Computing Machinery, 2020. [Online]. Available: <https://doi.org/10.1145/3400302.3415666>
- [54] C. Zhu, R. H. Byrd, P. Lu, and J. Nocedal, "Algorithm 778: L-bfgs-b: Fortran subroutines for large-scale bound-constrained optimization," *ACM Trans. Math. Softw.*, vol. 23, no. 4, p. 550–560, Dec. 1997. [Online]. Available: <https://doi.org/10.1145/279232.279236>